



Boosting hydrogen evolution of nickel phosphide by expanding built-in electric field with tungsten oxide

Xinyu Zhang ^{a,*}, Yiwen Dong ^b, Qianxi Lv ^b, Fuli Wang ^b, Chi Jiang ^a, Yingli Wang ^a, Jie Dou ^a, Qiyao Guo ^a, Bin Dong ^b, Qunwei Tang ^{a,*}

^a Institute of Carbon Neutrality, College of Chemical and Biological Engineering, Shandong University of Science and Technology, Qingdao 266590, PR China

^b State Key Laboratory of Heavy Oil Processing, College of Chemistry and Chemical Engineering, China University of Petroleum (East China), Qingdao 266580, PR China



ARTICLE INFO

Keywords:

Ni₂P/NF
WO₃
Built-in electric field
Alkaline medium
Hydrogen evolution reaction

ABSTRACT

Manipulating the built-in electric field (BIEF) in the catalyst to regulate the electronic structure and improve the carrier transport is a promising approach, but it is rarely applied in the design of hydrogen evolution reaction (HER) catalysts. In this study, the electrochemical microenvironment of nickel phosphide supported on nickel foam (Ni₂P/NF) has been modified by introducing tungsten oxide (WO₃) through simple ion group exchange strategy, thereby expanding the BIEF and enhancing the electron transport property. As a direct outcome, the target catalyst (20-WO₃/Ni₂P/NF) exhibits ultralow overpotential of 301 mV at high current density of ~1000 mA cm⁻². Additional characterization and density functional theory calculations demonstrate that the WO₃ can not only serve as a new hydrogen adsorption active site, but also effectively decrease the dissociation energy of water molecules at the nickel site, which results in rapid production and consumption of protons and enhancing the overall catalytic activity.

1. Introduction

The production of green hydrogen from renewable energy sources is regarded as an efficient and promising technology that can effectively achieve the goal of zero carbon emissions [1,2]. In general, the actual hydrogen production effect of this technique depends heavily on the selectivity, intrinsic activity and stability of the electrocatalyst applied for the water splitting [3,4]. Noble metal Pt-based materials show an almost perfect hydrogen adsorption Gibbs free energy ($\Delta G_H \approx 0$), but the HER rate of them in alkaline medium is several orders of magnitude lower than that under acidic electrolytes due to slow water dissociation process and poor proton supply [5–7]. In addition, the scarcity and high cost of Pt also severely limits its scale in practical applications [8,9]. Therefore, it is urgent to design and construct an electrocatalyst that can not only promote the rapid dissociation of water molecules in alkaline environment to produce sufficient hydrogen protons, but also possesses low cost, high reaction activity and long-term stability [10].

Transition metal nickel-based phosphide catalysts exhibit great potential in alkaline water electrolysis [11–14]. Among them, the Ni₂P has been reported to show the best HER activity, where the metal nickel can be used as an effective water dissociation site [15,16]. Especially when

combined with nickel foam (NF) with three-dimensional structure, the composed Mott Schottky (MS) heterostructure with suitable built-in electric field (BIEF) can further promote the carrier transport within it, thus showing excellent performance at high current density [17,18]. In general, the larger the BIEF, the stronger the degree of communication of current carrier between the metal and semiconductor, and the easier of the active site to regulate the electronic structure [19–21]. However, compared with precious metals, the lack of hydrogen adsorption sites makes it difficult to consume the dissociated protons quickly, resulting in a mismatch between them.

Interfacial chemistry plays an important role in improving the intrinsic catalytic activity of catalyst. Regulating the interfacial microenvironment, such as importing new modified species, can effectively control the strength of the built-in electric field and induce the charge transfer at the active site, which both has advantages of improving the water dissociation ability of nickel phosphide and introducing a new active site (hydrogen absorption/desorption), so as to solve the kinetic problem of proton consumption in alkaline environment [22–24]. In addition, the introduction of new species can also modify the BIEF of nickel phosphide, thereby enhancing the electron transport characteristics of the catalytic material, reducing the power loss in the electrolytic

* Corresponding authors.

E-mail addresses: skd994791@sdust.edu.cn (X. Zhang), tangqunwei@jnu.edu.cn (Q. Tang).

process and improving the electrolytic efficiency. Attribute to the rich reserves, adjustable composition, and high stability, tungsten oxide (WO_3) is considered to be one of the most attractive candidates among various HER catalysts. The abundant unsaturated bonds of W site can effectively accelerate the adsorption of the catalyst to the reaction intermediates, which makes it often act as an excellent component to further improve the hydrogen production performance of the main catalyst. If the WO_3 can be combined with $\text{Ni}_2\text{P}/\text{NF}$, the above-mentioned problems of proton consumption and electron structure regulation may be solved simultaneously. However, this promising strategy has rarely been reported, and the details of the experiment still remain to be explored.

Herein, a highly efficient HER electrocatalyst with dual sites was synthesized by a facile ion group exchange and low temperature phosphating strategy. By in situ electrochemical impedance spectroscopy (ITEIS) and MS measurement, it reveals that the introduction of tungsten oxide effectively regulates the BIEF of $\text{Ni}_2\text{P}/\text{NF}$, resulting in enhanced water dissociation effect and excellent electron transport properties. Density functional theory (DFT) calculations demonstrate that tungsten site in WO_3 can also be used as an excellent proton adsorption and consumption site to promote water electrolysis. Therefore, the 20- $\text{WO}_3/\text{Ni}_2\text{P}/\text{NF}$ electrode achieves remarkable hydrogen evolution activity (301 mV) and stability (100 h) at high current density (-1000 mA cm^{-2}). Meanwhile, owing to the advantages of mass and charge transfer, anion exchange membrane (AEM) water electrolyzer assembled by 20- $\text{WO}_3/\text{Ni}_2\text{P}/\text{NF}/\text{NF}$ can achieve 1000 mA cm^{-2} at 2.17 V and stably work for 100 h.

2. Experimental section

2.1. Chemicals

The nickel foam (NF) was obtained from Kunshan Guangjiayuan Electronics CO. LTD. Nitrate hexahydrate ($\text{Ni}(\text{NO}_3)_2 \cdot 6 \text{ H}_2\text{O}$, 98 %), sodium hypophosphate monohydrate ($\text{NaH}_2\text{PO}_2 \cdot \text{H}_2\text{O}$, 98 %), sodium tungstate dihydrate ($\text{Na}_2\text{WO}_4 \cdot 2 \text{ H}_2\text{O}$, 99.5 %), and potassium hydroxide (KOH, 85 %) were purchased from Sinopharm Chemical Reagent Co., Ltd. Deionized water with a resistivity of $18 \text{ M}\Omega \text{ cm}^{-1}$ was used in all reactions. All the chemicals were used without further purification.

2.2. Synthesis of $\text{NiNO}_3\text{OH}/\text{NF}$

$\text{NiNO}_3\text{OH}/\text{NF}$ was prepared by a molten salt method. Typically, 10 g $\text{Ni}(\text{NO}_3)_2 \cdot 6 \text{ H}_2\text{O}$ was added into a glass vial and heated it for 15 min at 85 °C. Then three pieces of cleaned NF (1 cm^2) were put into it for 60 min. After cooling down to room temperature, the resulting product was washed for several times with deionized water and dried by vacuum oven at 60 °C.

2.3. Synthesis of 20- $\text{NiWO}_x\text{OH}/\text{NF}$

For the typical preparation of 20- $\text{NiWO}_x\text{OH}/\text{NF}$, the prepared $\text{NiNO}_3\text{OH}/\text{NF}$ was immersed in 40 mL deionized water for 20 h. The obtained sample was then impregnated into the 0.01 M sodium tungstate solution for 1 h. In order to explore the influence of nitrate leaching, the different impregnation time was changed to obtain the n- $\text{NiWO}_x\text{OH}/\text{NF}$ ($n = 1, 5, 10$ and 50).

2.4. Synthesis of 20- $\text{WO}_3/\text{Ni}_2\text{P}/\text{NF}$

In a typical preparation of 20- $\text{WO}_3/\text{Ni}_2\text{P}/\text{NF}$, the obtained 20- $\text{WO}_x\text{OH}/\text{NF}$ product was put at one porcelain boat, and then 1 g $\text{NaH}_2\text{PO}_2 \cdot \text{H}_2\text{O}$ as phosphorus source was put at the other porcelain boat in the upstream side of the furnace. Subsequently, the two porcelain boats were calcined at 350 °C for 2 h with a heating speed of 2 °C min^{-1} under the Ar atmosphere. The n- $\text{WO}_3/\text{Ni}_2\text{P}/\text{NF}$ was synthesized as the

same method of 20- $\text{WO}_3/\text{Ni}_2\text{P}/\text{NF}$ except that the precursor was changed to n- $\text{WO}_x\text{OH}/\text{NF}$ ($n = 1, 5, 10$ and 50).

2.5. Materials characterizations

The X-ray diffraction (XRD) patterns were characterized on a JSM-7500 F diffractometer produced by JEOL. X-ray photoelectron spectroscopy (XPS) profiles were collected by A VG ESCALABMK II system with an Al K α radiator. The high-resolution transmission electron microscopy (HRTEM) images were obtained from FEI Tecnai G2 F20 S-TWIN. The scanning electron microscopy (SEM), SEM mapping and energy dispersive X-ray spectroscopy (EDS) were characterized through a Hitachi, S-4800. Inductive Coupled Plasma (ICP) characterization was conducted on an Agilent 720ES instrument.

2.6. Electrochemical measurements

All the electrochemical measurements were collected by Gamry Reference 1010 electrochemical workstation. Electrochemical performances of all catalysts were carried out with a standard three-electrode system in 1.0 M KOH. Where a saturated calomel electrode (SCE) and graphite rod were used as the reference electrode and the counter electrode, respectively. All the potentials involved in this work was referenced to reversible hydrogen electrode (RHE) with the Nernst equation: $E_{\text{RHE}} = E_{\text{SCE}} + 0.059 \text{ pH} + 0.245 \text{ V}$. For the HER performance, the linear sweep voltammetry (LSV) curves with iR-compensation were recorded at the potential range between -1 to -1.7 V vs. SCE at a scan rate of 2 mV s^{-1} . Electrochemical impedance spectroscopy (EIS) was analyzed at the same potential value with the frequency ranging from 100 kHz to 0.1 Hz under a voltage of 5 mV. The chronopotentiometric (CP) measurements were presented at a constant current density of -1000 mA cm^{-2} for 100 h. The TOF values of 20- $\text{WO}_3/\text{Ni}_2\text{P}/\text{NF}$ and $\text{Ni}_2\text{P}/\text{NF}$ were calculated by CV method, and the test potential range was ranging from -0.2 V to 0.6 V vs. RHE.

2.7. Electrochemical measurements in the AEM water electrolyzer

A Fumasep FAA-3-50 membrane was washed by 1 M KOH for 24 h at 25 °C for 24 h. The prepared 20- $\text{WO}_3/\text{Ni}_2\text{P}/\text{NF}$ and NF were used as cathode and anode catalysts with a geometric area of 1 cm^2 . Besides, the alkaline electrolyte (1 M KOH) was transported from the electrolyte pool to anode side by a self-priming pump. The performance evaluation of the AEM water electrolyzer using the electrocatalyst was performed by a Gamry Interface 1010 device. LSV curves were collected at a scan rate of 2 mV s^{-1} , typically between 1 and 2.2 V vs. RHE. The CP test was conducted at an industrial scale current density of 1000 mA cm^{-2} for up to 100 h.

2.8. Computation method

The density functional theory (DFT) calculations were performed by using the Vienna ab initio simulation package (VASP). The exchange correlation functional was treated with generalized gradient approximation of the Perdew-Burke-Ernzerh (GGA-PBE) functional. The cut-off energy was set to 570 eV for the plane-wave and the geometry optimizations were pursued until the force on each atom falls below the convergence criterion of 0.02 eV \AA^{-1} and energies were converged within 10^{-5} eV . The (111) crystal plane of Ni_2P and the (010) crystal plane of WO_3 were selected as the stable surface for subsequent DFT calculation. In addition, the vacuum spacing of Ni_2P and WO_3 surfaces perpendicular to the structural plane direction was 20 \AA . The free energy was calculated using the equation:

$$\Delta G = \Delta E_{\text{ads}} + \Delta ZPE - \Delta TS \quad (1)$$

where ΔG , ΔE_{ads} , ZPE and ΔTS were the free energy, total energy from

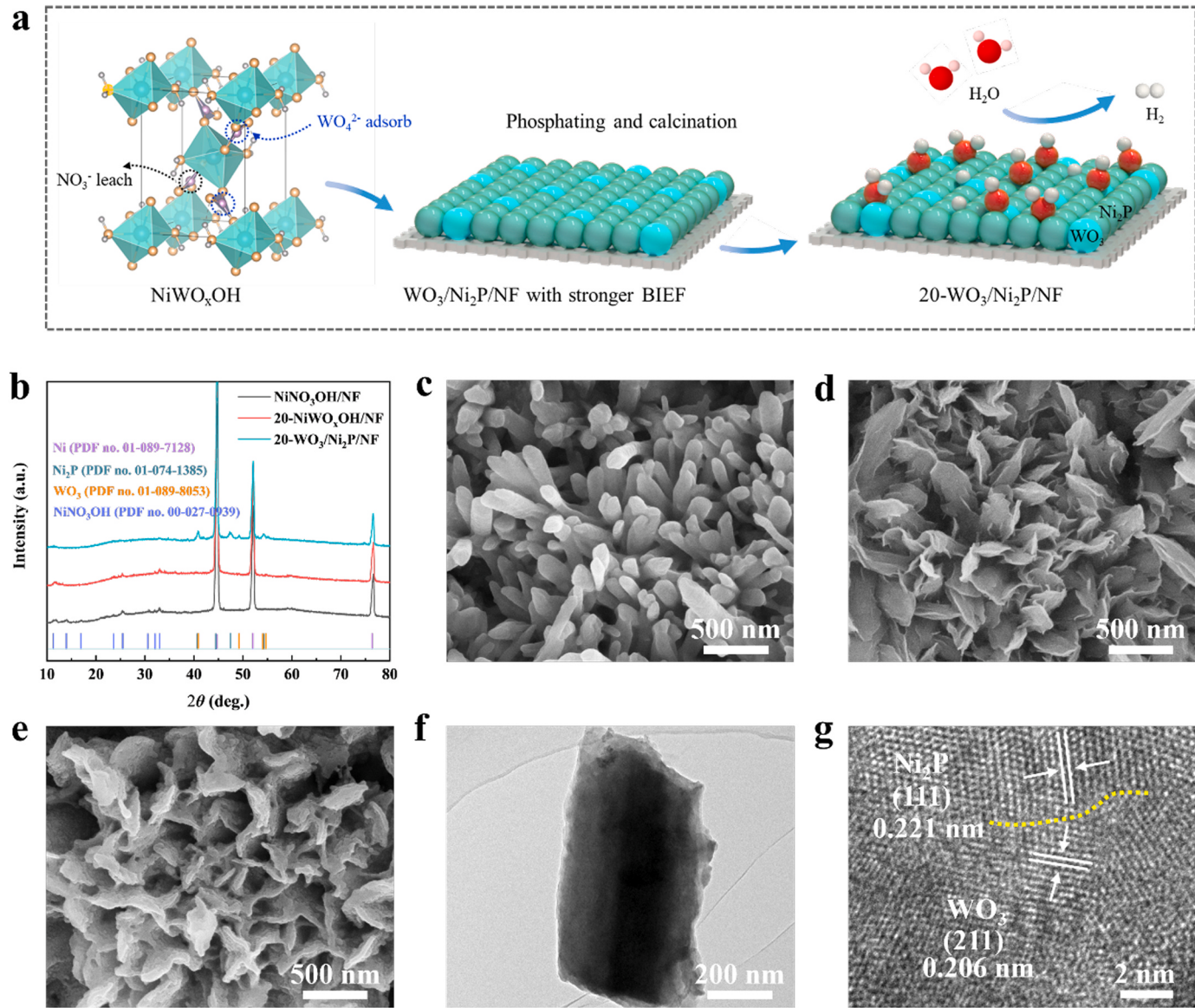


Fig. 1. (a) Schematic illustration of the synthesis process of $20\text{-WO}_3/\text{Ni}_2\text{P}/\text{NF}$ catalyst. (b) XRD patterns of the prepared $\text{NiNO}_3\text{OH}/\text{NF}$, $20\text{-NiWO}_x\text{OH}/\text{NF}$ and $20\text{-WO}_3/\text{Ni}_2\text{P}/\text{NF}$. Comparison of the SEM images of (c) $\text{NiNO}_3\text{OH}/\text{NF}$, (d) $20\text{-NiWO}_x\text{OH}/\text{NF}$ and $20\text{-WO}_3/\text{Ni}_2\text{P}/\text{NF}$. (f) HRTEM image of $20\text{-WO}_3/\text{Ni}_2\text{P}/\text{NF}$ catalyst. (g) HRTEM and corresponding FFT images of $20\text{-WO}_3/\text{Ni}_2\text{P}/\text{NF}$.

DFT calculations, zero-point energy and entropic contributions, respectively.

3. Results and discussion

3.1. Electrocatalyst preparation and characterization

As displayed in Fig. 1a, the $20\text{-WO}_3/\text{Ni}_2\text{P}$ nanosheet supported on nickel foam ($20\text{-WO}_3/\text{Ni}_2\text{P}/\text{NF}$) was synthesized by a facile combination of ion group exchange and gas phase phosphating. Here, the leaching of nitrate and the incorporation of tungstate were the key to realize the regulation of $\text{Ni}_2\text{P}/\text{NF}$ by WO_3 . Specifically, NiNO_3OH existed as a monoclinic, and Ni coordinated with four O and two OH to form an octahedral structure. Then, the N atom coordinated with three O and formed a plane triangle. At the junction of the two spatial configurations, Ni and N shared two oxygen atoms. When the NiNO_3OH precursor was immersed in aqueous solution, NO_3^- was easily dissolved and the imbalance of charge distribution of whole material would generate [25]. Finally, the WO_4^{2-} in the solution can be incorporated into the bulk phase

of NiNO_3OH in the form of adsorption. After the phosphating process, tungsten and nickel achieve the transformation to WO_3 and Ni_2P , respectively.

Fig. S1a was the optical photograph of NF, $\text{NiNO}_3\text{OH}/\text{NF}$, $\text{Ni}_2\text{P}/\text{NF}$ and $20\text{-WO}_3/\text{Ni}_2\text{P}/\text{NF}$. At each stage, the corresponding color has changed significantly. First, the crystal structures of $\text{NiNO}_3\text{OH}/\text{NF}$, $20\text{-NiWO}_x\text{OH}/\text{NF}$ and $20\text{-WO}_3/\text{Ni}_2\text{P}/\text{NF}$ were characterized by X-ray diffraction (XRD). As shown in Fig. 1b and Fig. S1b, in the initial $\text{NiNO}_3\text{OH}/\text{NF}$, almost pure NiNO_3OH (PDF No. 00-027-0939) was observed at around 10.9° , 13.7° , 16.7° , 25.2° , 30.4° , 32.2° and 32.8° , which can be indexed to (200), (002), (102), (−204), (210), (−310) and (310) crystal planes of it. After solution immersion (20 h) and tungstate ion exchange, the crystal phase structure of obtained sample ($20\text{-NiWO}_x\text{OH}/\text{NF}$) was basically similar to that of NiNO_3OH , indicating that the introduction of tungstate did not cause the main structure of the catalyst to collapse. When the $20\text{-NiWO}_x\text{OH}/\text{NF}$ was phosphating, the XRD spectrum of the hybrid sample exhibited a set of diffraction peaks, in which well-indexed peaks at 44.3° , 51.7° and 76.1° were assigned to Ni (PDF No. 01-089-7128), peaks at 41.1° , 49.1° , 54.2° and 55.2° were

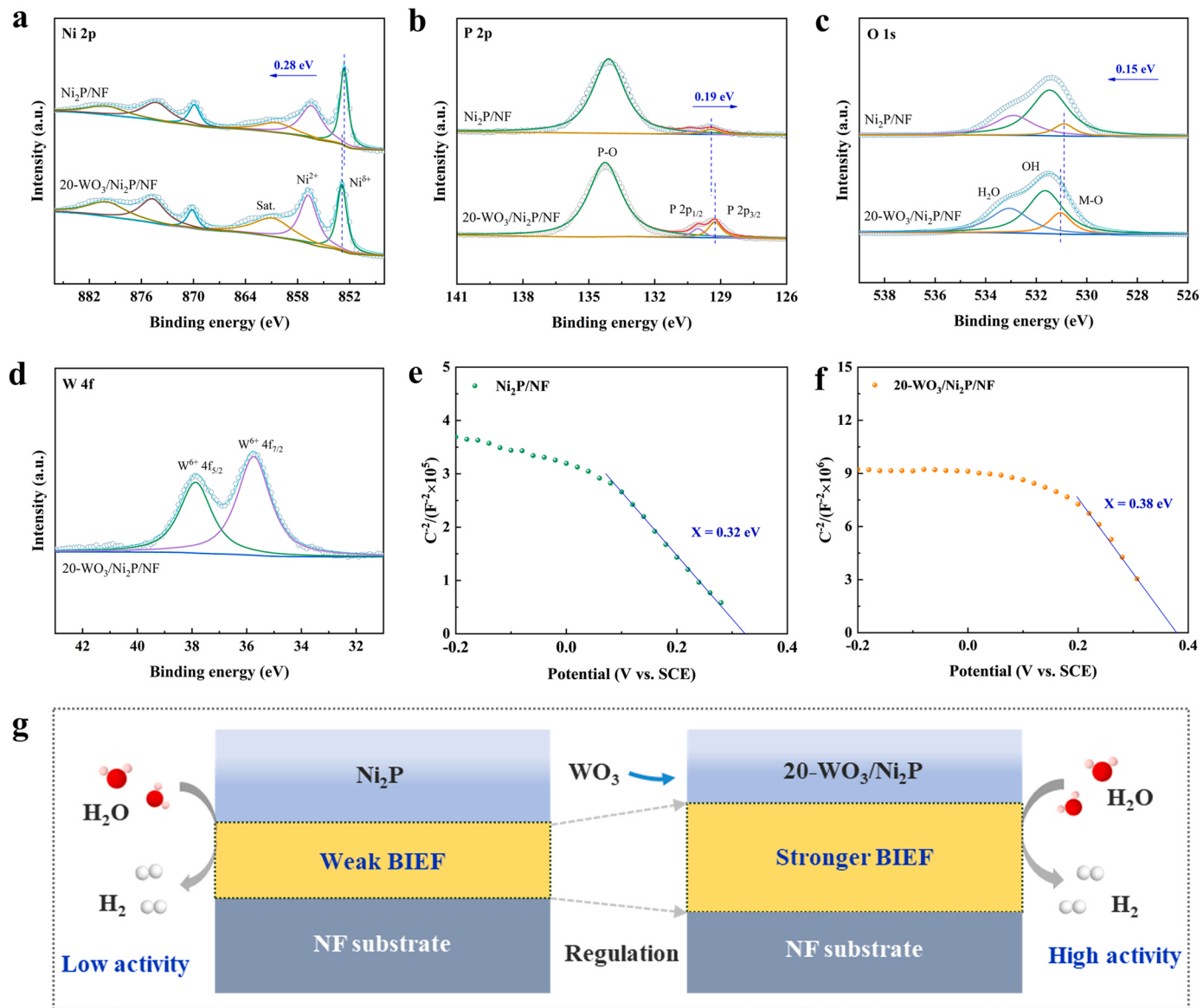


Fig. 2. High-resolution XPS patterns of (a) Ni 2p, (b) P 2p, (c) O 1 s and (d) W 2p in Ni₂P/NF and 20-WO₃/Ni₂P/NF catalyst. MS curves of (e) Ni₂P/NF and (f) 20-WO₃/Ni₂P/NF. (g) Schematic diagram of the BIEF and HER activity change for Ni₂P/NF and 20-WO₃/Ni₂P/NF catalyst.

ascribed to WO₃ (PDF No. 01-089-8053) and typical peaks at 40.8°, 44.7°, 47.3° and 54.3° were corresponded to Ni₂P (PDF No. 01-074-1385), respectively (Fig. S1c). The above results proved that the WO₃ was successfully introduced into Ni₂P/NF. The morphology of the catalyst was then characterized by scanning electron microscopy (SEM). As shown (Fig. S2 and Fig. 1c, d), in the SEM images of NiNO₃OH/NF and n-NiWO_xOH/NF (n represented immersion time; n = 1, 5, 10, 20 and 50) under the same magnification, the morphology of these materials has changed significantly from nanowires (NiNO₃OH/NF) to nanosheets (50-NiWO_xOH/NF) with the increased of impregnation time. After the phosphating process, the 20-WO₃/Ni₂P/NF was composed of similar sized and interconnected nanosheets (Fig. 1e). This layered structure could not only provide a multi-dimensional electron transport pathway, but also improve the mass transfer process in different catalytic processes. Transmission electron microscopy (TEM) further revealed the nanosheet structure of 20-WO₃/Ni₂P/NF with a diameter of 400 nm (Fig. 1f). High-resolution transmission electron microscopy (HRTEM) image showed that the crystal plane spacing of main lattice fringes was 0.221 nm, which corresponded to the (111) plane of Ni₂P. In addition, there were a small amount of crystalline structure (WO₃)

appeared in the middle of Ni₂P, indicating that tungsten oxide was successfully introduced to the edge of nickel phosphide (Fig. 1g) [25, 26]. The elemental mapping and composition of 20-WO₃/Ni₂P/NF catalyst was determined by energy dispersing spectrometer (EDS), which revealed that the Ni, P, O and W atoms were uniformly distributed and the ratio of them was 71.09: 17.60: 10.20: 1.11 (Fig. S3, Fig. S4 and Table. S1).

X-ray photoelectron spectroscopy (XPS) analysis was also applied to reveal the difference between Ni₂P/NF and 20-WO₃/Ni₂P/NF. In Fig. S5, the XPS survey exhibited the existence of Ni, O, P, and W elements on the surface of 20-WO₃/Ni₂P/NF. In contrast, the element of W was difficult to be detected in Ni₂P/NF, which corresponded to the results of SEM mapping. In high resolution spectrum of Ni 2p (Fig. 2a), peaks at 852.71 eV (Ni 2p_{3/2}) and 869.89 eV (Ni 2p_{1/2}) of Ni₂P/NF were corresponding to Ni⁸⁺ species (0 < δ < 2). While peaks at 856.4 eV (Ni 2p_{3/2}) and 874.4 eV (Ni 2p_{1/2}) of Ni₂P/NF was ascribed to Ni²⁺ [15, 27, 28]. After the phosphating progress, the peaks were shifted to higher binding energies (about 0.28 eV), which revealed the chemical binding between Ni₂P and WO₃ and testified the transfer of charge from Ni₂P to the WO₃. Therefore, the interfacial charge of 20-WO₃/Ni₂P/NF was redistributed,

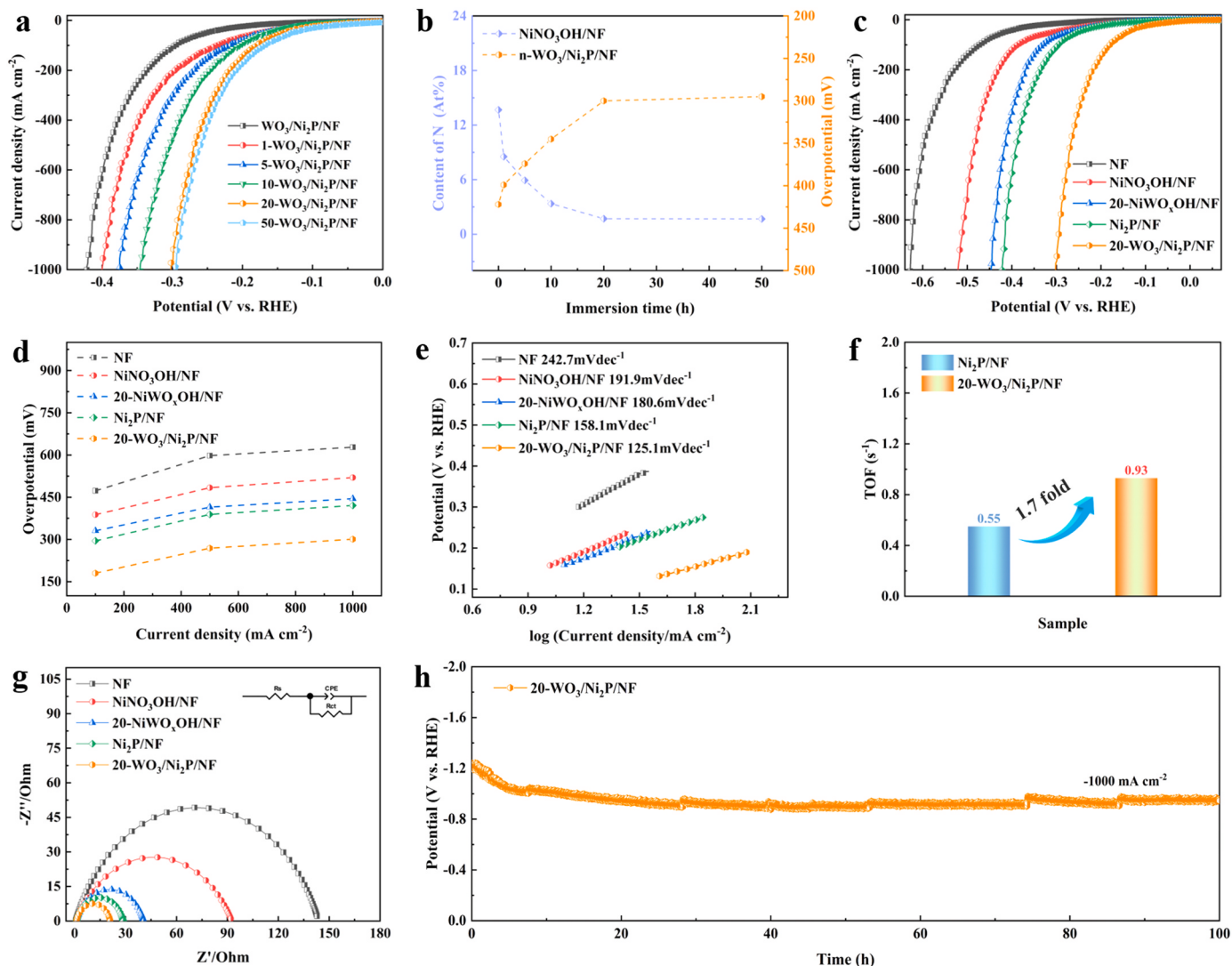


Fig. 3. (a) Polarization curves of n-WO₃/Ni₂P/NF with different immersion times for precursor. (b) The relationship between immersion times (precursor), N content (precursor) and overpotential of n-WO₃/Ni₂P/NF (-1000 mA cm⁻²). (c) Polarization curves of different catalysts. (d) Comparison of the overpotentials at -100, -500 and -1000 mA cm⁻². (e) Tafel plots. (f) Comparison of TOF at the overpotential of 300 mV for 20-WO₃/Ni₂P/NF and Ni₂P/NF. (g) The Nyquist plots of different samples. (h) Chronopotentiometry curve of 20-WO₃/Ni₂P/NF at a current density of -1000 mA cm⁻² for 100 h.

which was conducive to the intermediate adsorption during the water dissociation process. Subsequently, this charge change could also be reflected in the XPS spectrum of P 2p (Fig. 2b). As shown, compared with Ni₂P/NF, the P 2p peaks of 20-WO₃/Ni₂P/NF illustrated a negative shift (about 0.19 eV), indicating that the regulation of tungsten oxide increased the electron density of P at the interface [27,28]. In addition, O 1 s spectrum of 20-WO₃/Ni₂P/NF displayed that the content of M-O was significantly increased compared to Ni₂P/NF, (Fig. S6), further confirming the synthesis of tungsten oxide (Fig. 2c) [29]. Furthermore, the W 4 f spectra of 20-WO₃/Ni₂P/NF (Fig. 2d) could be clearly divided into two peaks as W⁶⁺ 4 f_{5/2} and W⁶⁺ 4 f_{7/2} at 37.88 and 35.73 eV, which was also corresponded to the valence state of tungsten in WO₃ [28,30].

As known, when Ni₂P was in contact with the NF, electrons and holes would undergo a mobile rearrangement and the BIEF could be formed at the contact interface. As the

nickel phosphide material on the surface of substrate was modified with tungsten oxide, the strength of BIEF would change correspondingly. Therefore, the change of electron configuration between Ni₂P/NF and 20-WO₃/Ni₂P/NF was determined by Mott-Schottky (MS) curve. And the formula of MS curve was as follows:

$$\frac{1}{C^2} = \frac{2}{\epsilon \epsilon_0 e N_d} (E - E_{fb} - \frac{k_B T}{e}) \quad (2)$$

Where C represented the space charge capacitance, ϵ and ϵ_0 were the permittivity of the semiconductor and the permittivity in vacuum, e was the electron charge and N_d was the carrier density [31,32]. In general, a positive slope in the MS diagram represented that the catalyst was an n-type semiconductor, while a negative slope implied that the sample was belonged to a p-type semiconductor [33]. Meanwhile, the intercept of the curve corresponded to the BIEF at the interface of the heterojunction. The larger the intercept indicated the stronger the degree of current carrier communication between the different components [34, 35]. As shown in Fig. 2e, when Ni₂P was loaded on the surface of NF, it displayed a negative slope value and small intercept (0.32 eV), indicating a typical p-type MS structure. After modification with WO₃, the intercept of 20-WO₃/Ni₂P/NF was further increased to 0.38 eV (Fig. 2f), indicating that the presence of tungsten oxide clearly enhanced the BIEF of Ni₂P/NF, which was more conducive to regulate the electronic structure and improve the reaction activity of Ni₂P/NF (Fig. 2g).

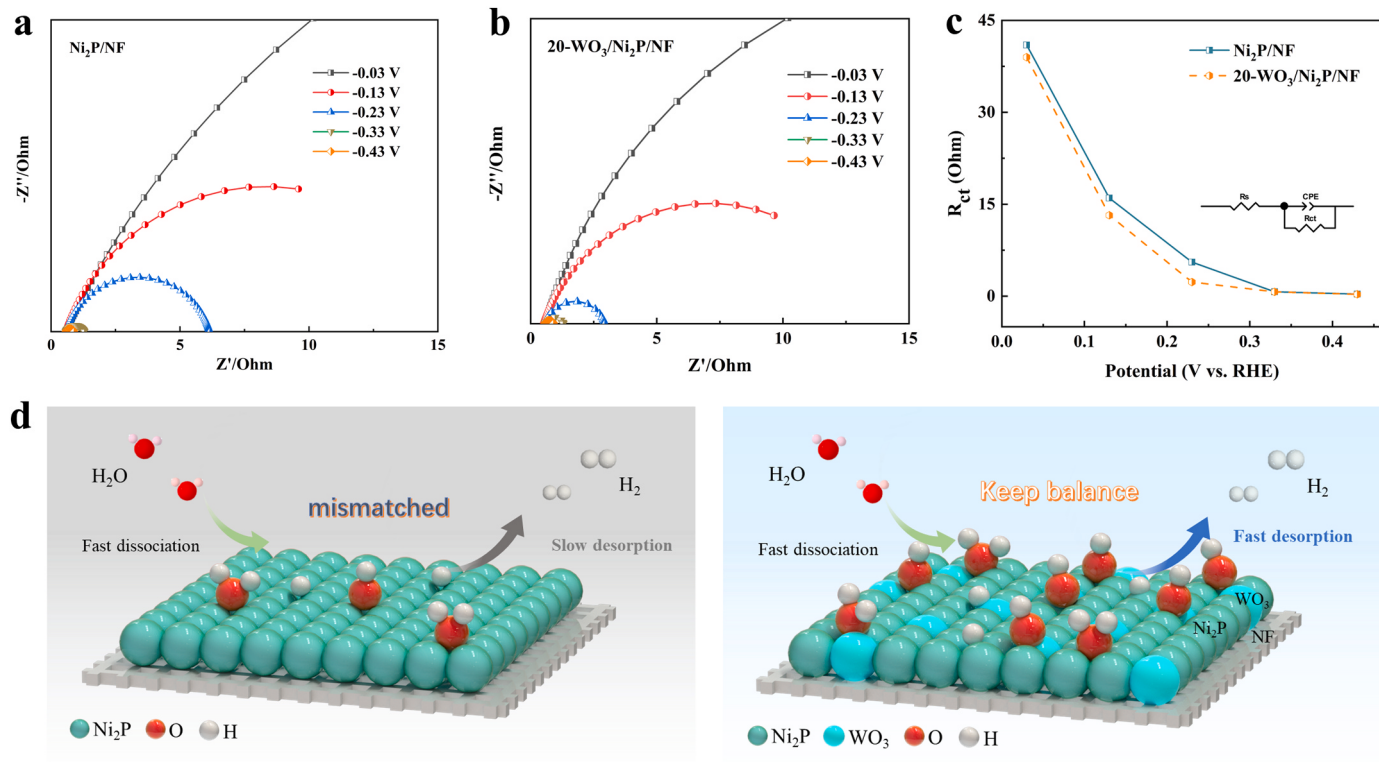


Fig. 4. Nyquist plots of water dissociation and hydrogen adsorption behavior for (a) $\text{Ni}_2\text{P}/\text{NF}$ and (b) $20\text{-WO}_3/\text{Ni}_2\text{P}/\text{NF}$. (c) The relationship between R_{ct} and applied potential for $\text{Ni}_2\text{P}/\text{NF}$ and $20\text{-WO}_3/\text{Ni}_2\text{P}/\text{NF}$. (d) Schematic of migration and evolution of water and hydrogen on the surface of $\text{Ni}_2\text{P}/\text{NF}$ and $20\text{-WO}_3/\text{Ni}_2\text{P}/\text{NF}$.

3.2. Electrocatalytic performance

To further investigate the effect of the tungsten incorporation content on the HER performance of catalyst, the relationship between immersion time (precursor), N content (precursor) and overpotential of $n\text{-WO}_3/\text{Ni}_2\text{P}/\text{NF}$ (-1000 mA cm^{-2}) was drawn. It could be seen that with the increased of the immersion time of the $\text{NiNO}_3\text{OH}/\text{NF}$ in solution, the content of N in it decreased significantly, indicating that the nitrate was dissolved during this process. When the solution contained tungstate, due to the charge balance, it would quickly occupy these vacant nitrate sites, thus achieving the subsequent modification of the electronic structure for nickel phosphide. Therefore, the longer the precursor soaking time, the higher the HER activity of $n\text{-WO}_3/\text{Ni}_2\text{P}/\text{NF}$. It

was worth noting that due to the maximum amount of nitrate leaching inside the precursor, there was an upper limit to the amount of tungstate in it (Fig. 3a, b). This result was also verified by ICP test of $n\text{-WO}_3/\text{Ni}_2\text{P}/\text{NF}$ ($n = 1, 5, 10, 20$ and 50). As shown in Table S2, the W content in catalyst has no longer increased significantly after the impregnation time reached 20 h. Considering the preparation cost and time consumption of the catalyst, the sample obtained after the precursor immersion for 20 h (basically the best performance) was further analyzed. The HER catalytic activity of all samples including NF, $\text{NiNO}_3\text{OH}/\text{NF}$, $20\text{-NiWO}_x\text{OH}/\text{NF}$, $\text{Ni}_2\text{P}/\text{NF}$ and $20\text{-WO}_3/\text{Ni}_2\text{P}/\text{NF}$ was then compared in 1 M KOH solution and the results were shown in Fig. 3c-h. As expected, the $20\text{-WO}_3/\text{Ni}_2\text{P}/\text{NF}$ catalyst always afforded the smallest η values and only needed of 180 , 269 and 301 mV to reach the current densities of -100 , -500 and -1000 mA cm^{-2} , which was better than those of NF ($\eta_{100} = 473 \text{ mV}$, $\eta_{500} = 598 \text{ mV}$ and $\eta_{1000} = 628 \text{ mV}$), $\text{NiNO}_3\text{OH}/\text{NF}$ ($\eta_{100} = 388 \text{ mV}$, $\eta_{500} = 484 \text{ mV}$ and $\eta_{1000} = 520 \text{ mV}$), $20\text{-NiWO}_x\text{OH}/\text{NF}$ ($\eta_{100} = 331 \text{ mV}$, $\eta_{500} = 415 \text{ mV}$ and $\eta_{1000} = 445 \text{ mV}$) and $\text{Ni}_2\text{P}/\text{NF}$ ($\eta_{100} = 295 \text{ mV}$, $\eta_{500} = 389 \text{ mV}$ and $\eta_{1000} = 421 \text{ mV}$) (Fig. 3c, d) and recent reported catalysts (Table S3). Fig. 3e displayed the Tafel plots of these catalysts. As revealed, the $20\text{-WO}_3/\text{Ni}_2\text{P}/\text{NF}$ exhibited a small Tafel slope of $\sim 125.1 \text{ mV dec}^{-1}$ in the region

of $\eta = 100\text{--}200 \text{ mV}$, which was much smaller than that of pure $\text{Ni}_2\text{P}/\text{NF}$ ($158.1 \text{ mV dec}^{-1}$), indicating that it followed a Volmer-Heyrovsky hydrogen evolution mechanism. This result also reflected that the electronic structure and reaction kinetics of Ni_2P was optimized after tungsten oxide regulation, which were consistent with the conclusion of XPS and BIEF. Next, the turnover frequency (TOF) was estimated at the overpotential of 300 mV , as depicted, the $20\text{-WO}_3/\text{Ni}_2\text{P}/\text{NF}$ showed a higher intrinsic activity (0.93 s^{-1}), which was 1.7 times than that of $\text{Ni}_2\text{P}/\text{NF}$ (0.55 s^{-1}) (Fig. 3f and Fig. S7). In addition, Nyquist plots were used to further analyze the electronic and mass transport of catalyst. It could be seen that $20\text{-WO}_3/\text{Ni}_2\text{P}/\text{NF}$ sample still possessed the smallest semicircle, indicating the lowest electron transfer impedance (Fig. 3g). It was worth noting that tungsten oxide itself was a semiconductor material, and when it was added to the main catalyst, the overall conductivity of the catalytic material would theoretically become worse. However, the charge transfer of $20\text{-WO}_3/\text{Ni}_2\text{P}/\text{NF}$ was well optimized after the introduction of WO_3 compared with pure $\text{Ni}_2\text{P}/\text{NF}$. These results revealed that the improvement of the conductivity of $20\text{-WO}_3/\text{Ni}_2\text{P}/\text{NF}$ was not originating from the addition of WO_3 with a new charge transfer channel, but came from the redistribution of electron configuration of the whole catalytic material caused by the modification of tungsten oxide on nickel phosphide. Subsequently, the stability of the $20\text{-WO}_3/\text{Ni}_2\text{P}/\text{NF}$ was evaluated at a current density of -1000 mA cm^{-2} . As shown in Fig. 3h, during the long-term stability test, the potential change of $20\text{-WO}_3/\text{Ni}_2\text{P}/\text{NF}$ could be negligible, indicating that the electrocatalytic performance of $20\text{-WO}_3/\text{Ni}_2\text{P}/\text{NF}$ was very stable. The characterizations including SEM, SEM mapping and EDS were further applied to investigate the change of $20\text{-WO}_3/\text{Ni}_2\text{P}/\text{NF}$ after the constant stability test. As illustrated, the $20\text{-WO}_3/\text{Ni}_2\text{P}/\text{NF}$ still retained an independent state and the elements of Ni, O, P and W were basically unchanged (Fig. S8, Fig. S9 and Table S4). However, the appearance of the nanosheet disappeared and became stronger nanorod, which might be caused by the edge of the nanosheet falling off. Fortunately, the three-dimensional cross-linked structure of the catalyst has been well

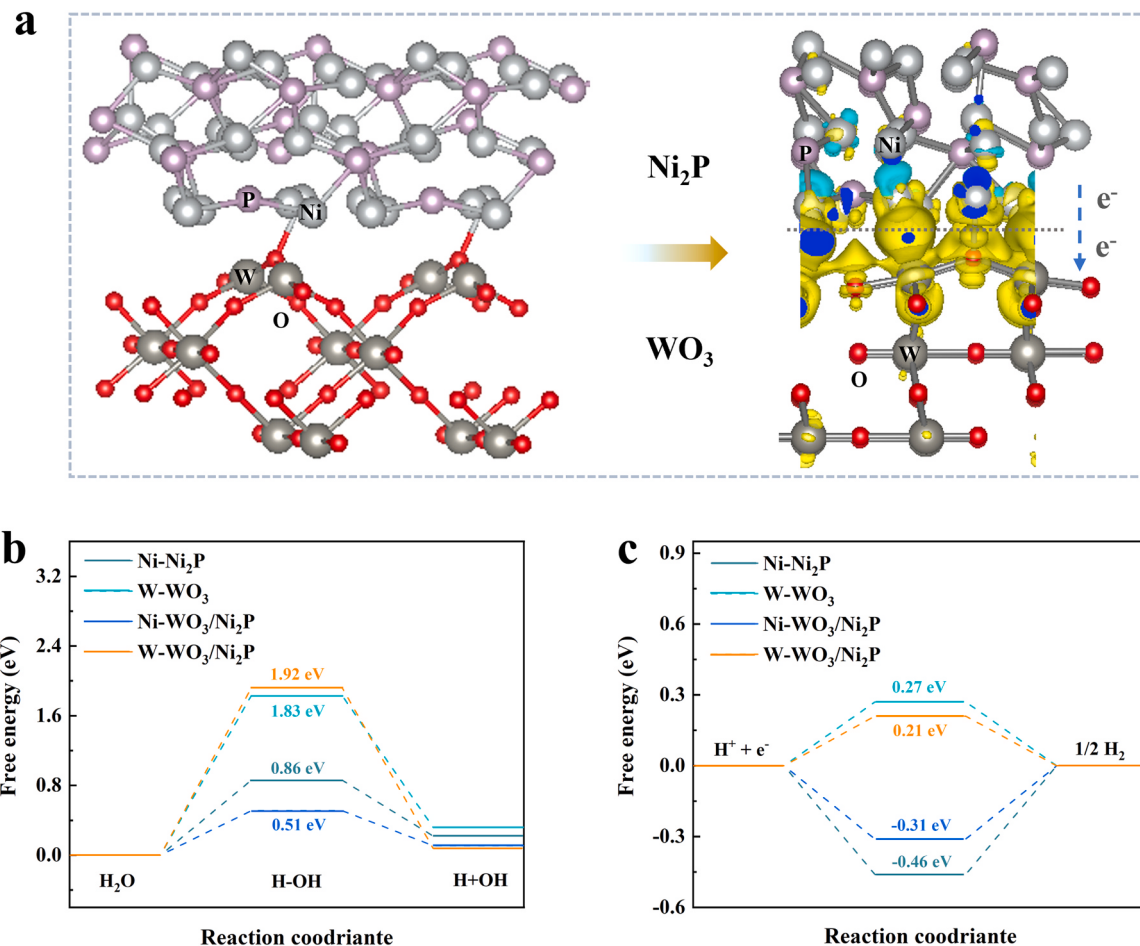


Fig. 5. (a) The optimized structural model of $\text{WO}_3/\text{Ni}_2\text{P}$ (left) and charge density difference diagram at the $\text{WO}_3/\text{Ni}_2\text{P}$ interface (right). (b) Free energy diagrams of water dissociation and (c) hydrogen adsorption on WO_3 , Ni_2P and $\text{WO}_3/\text{Ni}_2\text{P}$.

preserved, which greatly ensured that the catalytic structure would not collapse in the subsequent long-term water electrolysis process. In the case of no reduction in HER activity, this change might be considered favorable, which could not only reduce the actual cost of producing hydrogen, but also effectively reduce the pollution and damage of dissolved substances to the electrolyte and membrane components, thus giving it a large application potential.

For water splitting in alkaline environment, the dissociation and adsorption of water molecules and hydrogen atoms on the surface of catalyst were essential. Therefore, to further investigate the promotion behavior of the BIEF on the hydrogen evolution performance of $\text{Ni}_2\text{P}/\text{NF}$, *in situ* electrochemical impedance spectroscopy (ISEIS) was applied. Here, the Nyquist diagram was obtained under a series of different applied potentials. As shown in Fig. 4a-c, with the decreased of potential, the Faraday resistance of catalyst decreased and the surface reaction rate increased, which was consistent with HER process. Among them, the HER on 20- $\text{WO}_3/\text{Ni}_2\text{P}/\text{NF}$ showed a faster shrinkage tendency with the elevation of applied potential than that of $\text{Ni}_2\text{P}/\text{NF}$, indicating a stronger potential-dependent enhancement of charge-transfer rate [36, 37]. Those results revealed that the regulation of BIEF of $\text{Ni}_2\text{P}/\text{NF}$ by tungsten oxide could effectively promote the adsorption and consumption rate of water/hydrogen tend to balance, while their mismatched adsorption on $\text{Ni}_2\text{P}/\text{NF}$ restricted the consumption rate (Fig. 4d) [38].

3.3. Theoretical calculation

To further elucidate the promoting effect of tungsten oxide on nickel phosphide, density functional theory (DFT) calculation was applied.

According to XRD results and previous reports, the WO_3 (010) and Ni_2P (111) were selected to construct the stable $\text{WO}_3/\text{Ni}_2\text{P}$ interface structure (Fig. S10 and S11) [39,40]. The calculated charge density difference (Fig. 5a) showed the electron transfer process at the interface, where yellow and blue represented the accumulation and depletion of electrons on the surface of atom, respectively. It could be seen that the local charge redistribution induced electrons to move away from the Ni_2P surface, which was consistent with the results of XPS. In addition, the adsorption behavior of the reaction intermediates on the catalyst surface was analyzed. As revealed, the Gibbs free energy to dissociate a water molecule for Ni_2P (0.86 eV) and WO_3 (1.92 eV) were lower than that of $\text{WO}_3/\text{Ni}_2\text{P-Ni}$ (0.51 eV), indicating that Ni_2P could be used as an effective water dissociation site, and this ability could be further enhanced by tungsten oxide at the interface (Fig. 5b). Meanwhile, the calculation results showed that the dissociated H atom was preferentially adsorbing at the W site at the heterogeneous interface. And the Gibbs free energy of hydrogen for $\text{WO}_3/\text{Ni}_2\text{P}$ (0.21 eV) was the lowest among the three models (Fig. 5c). The above results further suggested that the introduction of tungsten oxide could not only serve as a new hydrogen adsorption site, but also modified the electronic structure of nickel phosphide, and thus promoting the electrolysis of water molecules in alkaline environment.

3.4. AEM water electrolyzer testing

Meanwhile, the feasibility of prepared HER catalyst in the electrolysis system was further evaluated in a AEM water electrolyzer (1 cm^2). Where the 20- $\text{WO}_3/\text{Ni}_2\text{P}/\text{NF}$ or $\text{Ni}_2\text{P}/\text{NF}$ was used as the cathode for

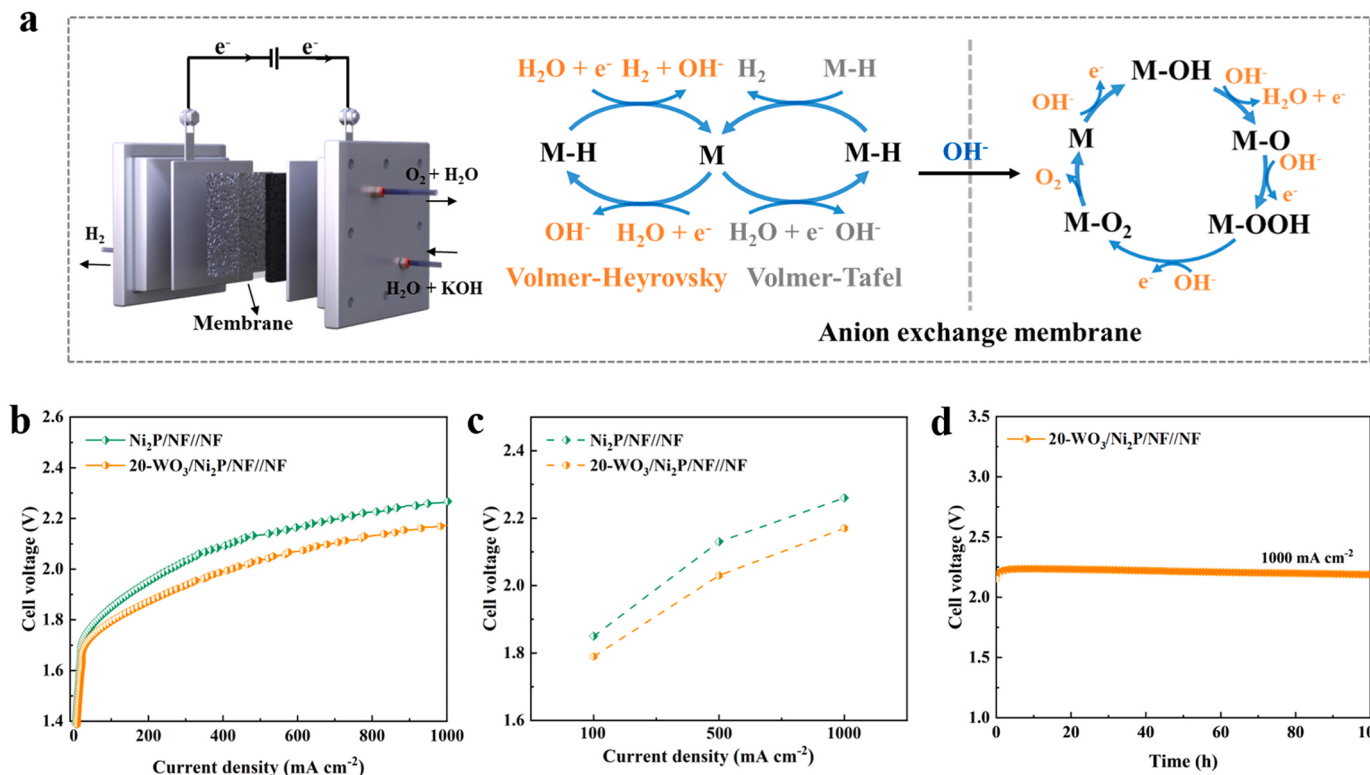


Fig. 6. The performance of the 20-WO₃/Ni₂P/NF catalyst in AEM water electrolyzer. (a) Schematic of the two-electrode AEM water electrolyzer using 20-WO₃/Ni₂P/NF or Ni₂P/NF and NF as cathode and anode. (b) Polarization curves of the 20-WO₃/Ni₂P/NF//NF and Ni₂P/NF//NF couple in an AEM single-cell. (c) Comparison of cell voltage at 100, 500 and 1000 mA cm⁻². (d) Chronopotentiometry curve of 20-WO₃/Ni₂P/NF//NF couple in KOH electrolyte.

HER and the NF was employed as the anode.

Meanwhile, the configuration and corresponding reaction mechanism of which was illustrated in Fig. 6a [41]. In Fig. 6b, the 20-WO₃/Ni₂P/NF//NF couple displayed an impressive current density of 100 mA cm⁻² at a 1.79 V battery voltage, which was lower than that of Ni₂P/NF//NF 1.85 V, reflecting the advanced nature of introducing WO₃ as a new hydrogen adsorption active site. As the current density increased, the 20-WO₃/Ni₂P/NF//NF still exhibited superior performance. When reached at 500 and 1000 mA cm⁻², it only needed low cell voltages of 2.03 and 2.17 V, respectively (Fig. 6c), outperforming the many recent reported AEM electrocatalysts (Table S5). Impressively, the AEM water electrolyzer with 20-WO₃/Ni₂P/NF//NF couple could also operate stably at an industrial-grade current density of 1000 mA cm⁻² with a competitive output cell voltage of 2.21 V for 20 h (Fig. 6d). The above phenomenon endowed the 20-WO₃/Ni₂P/NF a promising application prospect in the actual electrolytic water system in the future.

4. Conclusions

In conclusion, we have developed an effective ion-group exchange and low temperature phosphating strategy to construct a WO₃-regulated Ni₂P/NF catalytic materials. The modification of WO₃ could significantly expand the BIEF of Ni₂P/NF, thus regulating the electronic structure and promoting the rapid dissociation of water molecules on it. Meanwhile, the newly introduced WO₃ could also be used as the active site of hydrogen adsorption, making up for the difficult problem of adsorption and desorption of reaction intermediates on the surface of nickel phosphide. Attributing to the above advantages, the obtained 20-WO₃/Ni₂P/NF exhibited the superior HER activity (301 mV for -1000 mA cm⁻²) and durability (-1000 mA cm⁻² for 100 h) in 1 M KOH. For the scale production of hydrogen, the AEM water electrolyzer assembled by 20-WO₃/Ni₂P/NF//NF still demonstrated distinct advantage (1000 mA cm⁻² at 2.17 V, 1000 mA cm⁻² for 100 h). The method

of regulating the BIEF of catalyst by introducing new active site could effectively solve the problem of slow electrolysis of water kinetics in alkaline environment.

CRediT authorship contribution statement

Xinyu Zhang: Data curation, Writing – original draft, Formal analysis, Investigation, Writing – review & editing. **Yiwen Dong:** Writing – original draft, Conceptualization, Formal analysis, Writing – review & editing. **Qianxi Lv:** Writing – review & editing, Formal analysis. **Fuli Wang:** Writing – original draft, Formal analysis, Methodology. **Chi Jiang:** Writing – original draft, Formal analysis. **Yingli Wang:** Writing – review & editing, Formal analysis, Funding acquisition. **Jie Dou:** Writing – original draft, Writing – review & editing, Funding acquisition. **Qiyo Guo:** Writing – original draft, Formal analysis, Funding acquisition. **Bin Dong:** Conceptualization, Investigation, Resources, Formal analysis, Supervision, Writing – review & editing. **Qunwei Tang:** Formal analysis, Investigation, Resources, Writing – original draft, Funding acquisition, Project administration, Writing – review & editing.

Declaration of Competing Interest

The authors declare that they have no known competing financial interests or personal relationships that could have appeared to influence the work reported in this paper.

Data availability

Data will be made available on request.

Acknowledgements

This work was supported by National Key Research and

Development Program of China (2021YFE0111000), National Natural Science Foundation of China (62204098, 62304124, 22309107) and Shandong Provincial Natural Science Foundation (ZR202211290142).

Appendix A. Supporting information

Supplementary data associated with this article can be found in the online version at [doi:10.1016/j.apcatb.2023.123440](https://doi.org/10.1016/j.apcatb.2023.123440).

References

- [1] C. Feng, M. Lyu, J. Shao, H. Wu, W. Zhou, S. Qi, C. Deng, X. Chai, H. Yang, Q. Hu, C. He, Lattice strain engineering of Ni₂P enables efficient catalytic hydrazine oxidation-assisted hydrogen production, *Adv. Mater.* 10 (2023), 2305598.
- [2] H.Y. Wang, M.L. Sun, Z.Y. Yuan, Circumventing challenges: design of anodic electrocatalysts for hybrid water electrolysis systems, *Adv. Energy Mater.* 13 (2023), 2203568.
- [3] Z. Li, Y. Yue, J. Peng, Z. Luo, Phase engineering two-dimensional nanostructures for electrocatalytic hydrogen evolution reaction, *Chin. Chem. Lett.* 34 (2023), 107119.
- [4] H.Y. Wang, L. Wang, J.T. Ren, W.W. Tian, M.L. Sun, Z.Y. Yuan, Heteroatom-induced accelerated kinetics on nickel selenide for highly efficient hydrazine-assisted water splitting and Zn-hydrazine battery, *Nano Micro Lett.* 15 (2023) 155.
- [5] B. Zhu, R. Zou, Q. Xu, Metal-organic framework based catalysts for hydrogen evolution, *Ad. Energy Mater.* 8 (2018), 1801193.
- [6] X. Xu, Y. Chen, W. Zhou, Z. Zhu, C. Su, M. Liu, Z. Shao, A. Perovskite, Electrocatalyst for efficient hydrogen evolution reaction, *Adv. Mater.* 28 (2016) 6442–6448.
- [7] S. Chen, J. Liao, Z. Zhou, S. Yang, Q. Gao, X. Cai, F. Peng, Y. Fang, S. Zhang, Boosting photocatalytic hydrogen evolution using a noble-metal-free co-catalyst: CuNi@C with oxygen-containing functional groups, *Appl. Catal. B Environ.* 291 (2021), 120139.
- [8] W. Liang, M. Zhou, X. Lin, J. Xu, P. Dong, Z. Le, M. Yang, J. Chen, F. Xie, N. Wang, Y. Jin, H. Meng, Nickel-doped tungsten oxide promotes stable and efficient hydrogen evolution in seawater, *Appl. Catal. B Environ.* 325 (2023), 122397.
- [9] J. Zhang, Y. Liu, C. Sun, P. Xi, S. Peng, D. Gao, D. Xue, Accelerated hydrogen evolution reaction in CoS₂ by transition-metal doping, *ACS Energy Lett.* 3 (2018) 779–786.
- [10] H.M. Yang, H.Y. Wang, M.L. Sun, Z.Y. Yuan, Interface engineering of bifunctional nickel hydroxide/nickel phosphide heterostructure for efficient intermittent hydrazine-assisted water splitting, *Chem. Eng. J.* 475 (2023), 146434.
- [11] D.L. Wu, B. Liu, R.D. Li, D. Chen, W.H. Zeng, H.Y. Zhao, Y.T. Yao, R. Qin, J. Yu, L. Chen, J.N. Zhang, B. Li, S.C. Mu, Fe-regulated amorphous-crystal Ni(Fe)P₂ nanosheets coupled with Ru powerfully drive seawater splitting at large current density, *Small* 19 (2023), 2300030.
- [12] D. Chen, H.W. Bai, J.W. Zhu, C. Wu, H.Y. Zhao, D.L. Wu, J.X. Jiao, P.X. Ji, S.C. Mu, Multiscale hierarchical structured NiCoP enabling ampere-level water splitting for multi-scenarios green energy-to-hydrogen systems, *Adv. Energy Mater.* 13 (2023), 202300499.
- [13] H.M. Yang, H.Y. Wang, M.L. Sun, Z.Y. Yuan, Multifunctional metal-phosphide-based electrocatalysts for highly efficient solar hydrogen production integrated devices, *J. Mater. Chem. A* 11 (2023) 2899–2909.
- [14] H.M. Yang, H.Y. Wang, M.L. Sun, Z.Y. Yuan, Synergistically enhanced activity and stability of bifunctional nickel phosphide/sulfide heterointerface electrodes for direct alkaline seawater electrolysis, *J. Energy Chem.* 75 (2022) 66–73.
- [15] D.N. Nguyen, T.K.C. Phu, J. Kim, W.T. Hong, J.S. Kim, S.H. Roh, H.S. Park, C. H. Chung, W.S. Choe, H. Shin, J.Y. Lee, J.K. Kim, Interfacial strain-modulated nanospherical Ni₂P by heteronuclei-mediated growth on Ti₃C₂T_x MXene for efficient hydrogen evolution, *Small* 18 (2022), 2204797.
- [16] H.W. Bai, D. Chen, Q.L. Ma, R. Qin, H.W. Xu, Y.F. Zhao, J.X. Chen, S.C. Mu, Atom doping engineering of transition metal phosphides for hydrogen evolution reactions, *Electrochem. Energy Rev.* 5 (2022), 24, <https://doi.org/10.1007/s41918-022-00161-7>.
- [17] Y.W. Dong, H.J. Liu, X. Wang, F.L. Wang, X.Y. Zhang, Q.X. Lv, C.Y. Liu, Y.M. Chai, B. Dong, Manganese doping regulated the built-in electric field of FeBTC for enhanced photoelectrocatalytic hydrolysis, *Appl. Catal. B Environ.* 328 (2023), 122464.
- [18] J. Zhang, H. Yu, J. Yang, X. Zhu, M. Hu, J. Yang, Heterostructure engineering of the Fe-doped Ni phosphides/Ni sulfide p-p junction for high-efficiency oxygen evolution, *J. Alloy. Compd.* 924 (2022), 166613.
- [19] Y. Kang, S. Wang, K.S. Hui, S. Wu, D.A. Dinh, X. Fan, F. Bin, F. Chen, J. Geng, W.C. M. Cheong, K.N. Hui, Surface reconstruction establishing Mott-Schottky heterojunction and built-in space-charging effect accelerating oxygen evolution reaction, *Nano Res.* 15 (2022) 2952–2960.
- [20] M. Yuan, J. Chen, Y. Bai, Z. Liu, J. Zhang, T. Zhao, Q. Wang, S. Li, H. He, G. Zhang, Unveiling electrochemical urea synthesis by co-activation of CO₂ and N₂ with Mott-Schottky heterostructure catalysts, *Angew. Chem. Int. Ed.* 60 (2021) 10910–10918.
- [21] S. Zhang, C. Zhang, X. Zheng, G. Su, H. Wang, M. Huang, Integrating electrophilic and nucleophilic dual sites on heterogeneous bimetallic phosphide via enhancing interfacial electronic field to boost hydrazine oxidation and hydrogen evolution, *Appl. Catal. B Environ.* 324 (2023), 122207.
- [22] J.W. Zhu, S.C. Mu, Parsing the basic principles to build efficient heterostructures toward electrocatalysis, *Inorg. Chem. Front.* 10 (2023) 2220–2225.
- [23] D. Chen, R.H. Lu, R.H. Yu, Y.H. Dai, H.Y. Zhao, D.L. Wu, P.Y. Wang, J.W. Zhu, Z. H. Pu, L. Chen, J. Yu, S.C. Mu, Work-function-induced Interfacial Built-in electric fields in Os-OsSe₂ heterostructures for active acidic and alkaline hydrogen evolution, *Angew. Chem. Int. Ed.* 61 (2022), 2208642.
- [24] H.R. Inta, S. Ghosh, A. Mondal, G. Tudu, H. Koppisetti, V. Mahalingam, Ni_{0.85}Se/MoSe₂ interfacial structure: an efficient electrocatalyst for alkaline hydrogen evolution reaction, *ACS Appl. Energy Mater.* 4 (2021) 2828–2837.
- [25] Y.N. Zhou, Y.W. Dong, Y. Wu, B. Dong, H.J. Liu, X.J. Zhai, G.Q. Han, D.P. Liu, Y. M. Chai, Nitrate induced precise atom substitution and vacancies for overall water splitting, *Chem. Eng. J.* 463 (2023), 142380.
- [26] Z.Y. Yu, Y. Duan, J.D. Liu, Y. Chen, X.K. Liu, W. Liu, T. Ma, Y. Li, X.S. Zheng, T. Yao, M.R. Gao, J.F. Zhu, B.J. Ye, S.H. Yu, Unconventional CN vacancies suppress iron-leaching in prussian blue analogue pre-catalyst for boosted oxygen evolution catalysis, *Nat. Commun.* 10 (2019) 2799.
- [27] J.T. Ren, L. Wang, L. Chen, X.L. Song, Q.H. Kong, H.Y. Wang, Z.Y. Yuan, Interface metal oxides regulating electronic state around nickel species for efficient alkaline hydrogen electrocatalysis, *Small* 19 (2023), 2206196.
- [28] H.M. Yang, H.Y. Wang, M.L. Sun, Z.Y. Yuan, Synergistic activation of crystalline Ni₂P and amorphous NiMoO_x for efficient water splitting at high current densities, *ACS Catal.* 13 (2023) 9792–9805.
- [29] X. Ren, J. Shi, R. Duan, J. Di, C. Xue, Y. Luo, Q. Liu, M. Xia, B. Lin, W. Tang, Construction of high-efficiency CoS@Nb₂O₅ heterojunctions accelerating charge transfer for boosting photocatalytic hydrogen evolution, *Chin. Chem. Lett.* 33 (2022) 4700–4704.
- [30] W. Liu, H. Zhang, M. Ma, D. Cao, D. Cheng, Constructing a highly active amorphous WO₃/crystalline CoP interface for enhanced hydrogen evolution at different pH values, *ACS Appl. Energy Mater.* 5 (2022) 10794–10801.
- [31] Y.W. Dong, F.L. Wang, Y. Wu, X.J. Zhai, N. Xu, X.Y. Zhang, R.Q. Lv, Y.M. Chai, B. Dong, Directed electron regulation promoted Sandwich-like CoO@FeBTC/NF with p-n heterojunctions by gel electrodeposition for oxygen evolution reaction, *J. Colloid Interface Sci.* 645 (2023) 410–419.
- [32] L. Chen, J.T. Ren, Z.Y. Yuan, Enabling internal electric fields to enhance energy and environmental catalysis, *Adv. Energy Mater.* 13 (2023), 2203720.
- [33] S. Hamrouni, M.S. AlKhalifah, M.S. El-Bana, S.K. Zobaidi, S. Belgacem, Deposition and characterization of spin-coated n-type ZnO thin film for potential window layer of solar cell, *Appl. Phys. A* 124 (2018) 555.
- [34] C. Guo, B. Wu, S. Ye, J. Liu, X. Deng, L. Luo, Q. Li, X. Xiao, J. Wang, J. Liu, T. Xia, B. Jiang, Enhancing the heterojunction component-interaction by In-Situ hydrothermal growth toward photocatalytic hydrogen evolution, *J. Colloid Interface Sci.* 614 (2022) 367–377.
- [35] X. Zhao, M. Liu, Y. Wang, Y. Xiong, P. Yang, J. Qin, X. Xiong, Y. Lei, Designing a built-in electric field for efficient energy electrocatalysis, *ACS Nano* 16 (2022) 19959–19979.
- [36] Q. Wen, J. Duan, W. Wang, D. Huang, Y. Liu, Y. Shi, J. Fang, A. Nie, H. Li, T. Zhai, Engineering a local free water enriched microenvironment for surpassing platinum hydrogen evolution activity, *Angew. Chem. Int. Ed.* 61 (2022), e202206077.
- [37] X. Tong, Y. Zhao, Z. Zhuo, Z. Yang, S. Wang, Y. Liu, N. Lu, H. Li, T. Zhai, Dual-regulation of defect sites and vertical conduction by spiral domain for electrocatalytic hydrogen evolution, *Angew. Chem. Int. Ed.* 61 (2022) 202112953.
- [38] H. Yang, Y. Zhao, Q. Wen, Y. Mi, Y. Liu, H. Li, T. Zhai, Single MoTe₂ sheet electrocatalytic microdevice for in situ revealing the activated basal plane sites by vacancies engineering, *Nano Res.* 14 (2021) 4814–4821.
- [39] X. Wang, Q. Hu, G. Li, S. Wei, H. Yang, C. He, Regulation of the adsorption sites of Ni₂P by Ru and S co-doping for ultra-efficient alkaline hydrogen evolution, *J. Mater. Chem. A* 9 (2021) 15648–15653.
- [40] T. Zheng, W. Sang, Z. He, Q. Wei, B. Chen, H. Li, C. Cao, R. Huang, X. Yan, B. Pan, S. Zhou, J. Zeng, Conductive tungsten oxide nanosheets for highly efficient hydrogen evolution, *Nano Lett.* 17 (2017) 7968–7973.
- [41] H. Jin, B. Ruqia, Y. Park, H.J. Kim, H.S. Oh, S.I. Choi, K. Lee, Nanocatalyst design for long-term operation of proton/anion exchange membrane water electrolysis, *Adv. Energy Mater.* 11 (2021), 2003188.